Research Square

Preprints are preliminary reports that have not undergone peer review.
They should not be considered conclusive, used to inform clinical practice,
or referenced by the media as validated information.

Biomechanical performance of a new tantalum artificial vertebral body after total en bloc spondylectomy of the C5 segment: A finite element study

Yutao Zhang
Xinjiang institute of engineering
Wurikaixi Aiyiti
wurikaixi@xju.edu.cn
Xinjiang University
Jintao Li
Xinjiang institute of engineering
Yong Teng
Hospital of Xinjiang Military Region PLA

Research Article

Keywords: Artificial vertebral body, Biomechanical, Finite element analysis, Tantalum, Total en bloc spondylectomy

Posted Date: November 23rd, 2026

DOI: https://doi.org/10.21203/rs.3.rs-10715817/v1

License: This work is licensed under a Creative Commons Attribution 4.0 International License.
Read Full License

Additional Declarations: No competing interests reported.

Biomechanical performance of a new tantalum artificial vertebral body after total en bloc spondylectomy of the C5 segment: A finite element study

Yutao Zhang [1], Wurikaixi Aiyiti [2]*, Jintao Li [1,2], Yong Teng [3]**

[1] Xinjiang Coal Mine Electromechanical Engineering Technology Research Center, School of Electromechanical Engineering, Xinjiang institute of engineering, Urumqi, Xinjiang, PR China

[2] School of Mechanical Engineering, Xinjiang University, Urumqi, Xinjiang, PR China

[3] Department of Orthopaedics, Hospital of Xinjiang Military Region PLA, Urumqi, PR. China.

*Corresponding author:

Wurikaixi Aiyiti, School of Mechanical Engineering, Xinjiang University, Urumqi, PR. China.

E-mail address: wurikaixi@xju.edu.cn (W. Aiyiti).

**Co-corresponding author:

Yong Teng, Department of Orthopaedics, Hospital of Xinjiang Military Region PLA, Urumqi, PR. China.

E-mail address: orthtengyong@163.com (Yong T.).

Biomechanical performance of a new tantalum artificial vertebral body after total en bloc spondylectomy of the C5 segment: A finite element study

ABSTRACT

Background

Total en bloc spondylectomy treats cervical spine tumors by removing the diseased vertebrae, implanting a titanium mesh cage (TMC) and posterior fixation. There is a significant risk of subsidence associated with TMC, necessitating the development of a novel customized artificial vertebral body (AVB) to replace TMC, thereby achieving improved clinical outcomes.

Methods

This study aimed to examine the biomechanical performance of TMC and tantalum AVB and to evaluate the feasibility of their clinical application. Three novel tantalum artificial vertebral bodies (AVB-1, AVB-2, and AVB-3) were customized designed using topology optimization combined with lattice structure design. The effects of TMC, AVB, and pedicle screw rods on the range of motion, contacting vertebrae, adjacent intervertebral discs, and articular cartilage were investigated using finite element analysis (FEA).

Results

It was difficult for TMC and AVB-1 to provide long-term stability for cervical fusion because of insufficient stiffness. The stress-shielding effect of AVB-3 was significant owing to its high stiffness. AVB-2 had a good load-bearing capacity and moderate stiffness under all motions. This significantly reduced the stress-masking effect on the adjacent segments and provided long-term stability for cervical fusion.

Conclusion

AVB-2 is an optimal artificial vertebral body design option with potential clinical applications.

Keywords: Artificial vertebral body, Biomechanical, Finite element analysis, Tantalum, Total en bloc spondylectomy

1. Introduction

Total en bloc spondylectomy (TES) has become the preferred treatment option for spinal tumors because of its good local control and long survival cycles. [1] This procedure reconstructs the anterior column by implanting a titanium (Ti) mesh cage and combining it with posterior fixation to restore spinal stability. [2] However, some clinical reports have indicated that Ti mesh cage implantation is prone to vertebral body collapse and subsidence. [3-5] Severe cage subsidence may result in complications, including the loss of intervertebral height, neurological damage, and fusion failure. Recently, researchers have attempted to develop customized artificial vertebral bodies to replace Ti mesh cages for better clinical outcomes. [6-10] Custom design involves optimizing the material and structure of an artificial vertebral body according to the specific shape and anatomical dimensions of a patient's vertebrae.

Titanium is extensively employed in orthopedic implants due to its superior mechanical stability, biocompatibility, and resistance to corrosion. [11-13] Poly-ether-ether-ketone (PEEK), characterized by an elastic modulus similar to that of human bone, [14, 15] has gained popularity in recent years as a material suitable for spinal implants. [16-18] However, the bioactivity of PEEK is insufficient, limiting its clinical application. [19-21] Tantalum (Ta) has superior biocompatibility compared with Ti. [22-24] The Ta_2O_5 on its surface exhibits good osteoinductive and antimicrobial properties. [25] Therefore, after implantation into the body, the Ta artificial vertebral body had a higher potential for osseointegration than the Ti artificial vertebral body. With elastic moduli of 186 GPa and 110 GPa, tantalum (Ta) and titanium (Ti) exhibit significantly higher stiffness compared to human bone, which ranges from 0.022 to 21 GPa. [26] The vertebral prosthesis induces stress shielding of the vertebra, thereby inhibiting its fusion with the surrounding bone tissue. [27]

The porous structural design of a solid Ta artificial vertebral body is an effective method for reducing its elastic modulus. [28, 29] The lattice structure is a distinct porous material characterized by a systematic arrangement of multiple unit cells. Compared to random porous structures, lattice structures have the advantages of controllable mechanical properties and pore structures. [30, 31] The mechanical properties of the lattice,

specifically its elastic modulus and yield strength, can be aligned with those of the human bone by adjusting the design parameters. These parameters include the selection of the unit cell type, degree of porosity, and strut diameter, all of which are critical for reducing the risk of stress shielding. [32-34] Furthermore, cell and bone tissue growth can be promoted by regulating the pore structure of the lattice, such as the pore shape and diameter. [35-37] During the structural design process, the curvature and height of the upper and lower end surfaces of the artificial vertebral body are made consistent with the curvature and intervertebral height of the endplate of the vertebral body, respectively. By alleviating the stress concentration at the contact interface, the likelihood of subsidence in artificial vertebral bodies is diminished. [38-40]

The development of additive manufacturing has provided more freedom for customized design of artificial vertebral bodies. Selective laser melting (SLM) is a technique that employs a high energy input and precise molding to manufacture tantalum (Ta) artificial vertebral bodies with complex geometries. [27, 41] According to our previous study, [42, 43] the mechanical properties of Ta artificial vertebral body samples could be assessed using a quasi-static compression test. However, it is very difficult to verify the biomechanical performance of artificial vertebrae after implantation in the human body through tests, owing to the complexity of clinical trials. Finite element analysis (FEA) is extensively employed in biomechanical research on spinal implants. [44-49] Through the application of FEA, researchers can evaluate how stresses and strains are distributed across vertebral bones, intervertebral discs, articular cartilage, artificial vertebral bodies, and other anatomical structures. This assessment is performed during typical loading and movement following the implantation of an artificial vertebral body in the human body. This approach offers a systematic means of analyzing the influence of Ta artificial vertebral bodies and pedicle screw rods on both the fused and adjacent spinal segments. It also facilitates the assessment of the clinical potential of Ta artificial vertebral bodies. In the present study, three innovative Ta artificial vertebral bodies were specifically designed to align with the anatomical dimensions of the human cervical spine. The proposed design methodology integrates topology optimization with lattice structure design. The effects of Ti mesh, artificial vertebral bodies, and pedicle screw rods on

ROM, contacting vertebrae, adjacent intervertebral discs, and articular cartilage were investigated using finite element analysis. Load transfer patterns between the artificial vertebral bodies and pedicle screw rods were analyzed. This study aimed to investigate the biomechanical properties of Ta artificial vertebral bodies post-implantation in the human body, employing finite element analysis for evaluation. Additionally, the study sought to compare the mechanical properties of these Ta artificial vertebral bodies with those of the conventional Ti mesh cage and to evaluate the feasibility of their clinical application.

2. Materials and methods

2.1 Intact cervical spine C3-C7 model

A solid three-dimensional model representing the C3-C7 segments was constructed based on the computed tomography (CT) data obtained from the human cervical spine (height: 179 cm and weight: 73 kg; NeuViz Glory CT, Neusoft, China). The scanning thickness was set to 1mm. The intact C3-C7 cervical segment model and the model after TES are shown in **Figure 1**. The intact model included five vertebral segments, four intervertebral discs, four pairs of articular cartilages, and 36 ligaments. As shown in **Figure 1**, the vertebral segment comprises cortical bone, cancellous bone, and facet joints. The cortical bone and articular cartilage were 0.5 and 2 mm thick, respectively. The intervertebral disc includes two endplates, an annulus fibrosus, and a nucleus pulposus. The volume ratio of the nucleus pulposus to the annulus fibrosus was approximately 2:3, and the endplate thickness was 0.5 mm. The ligaments that connect the vertebral segments comprise the ligamentum flavum (LF), supraspinal ligament (SSL), anterior longitudinal ligament (ALL), interspinal ligament (ISL), capsular ligaments (CL), intertransverse ligament (ITL), and posterior longitudinal ligament (PLL).

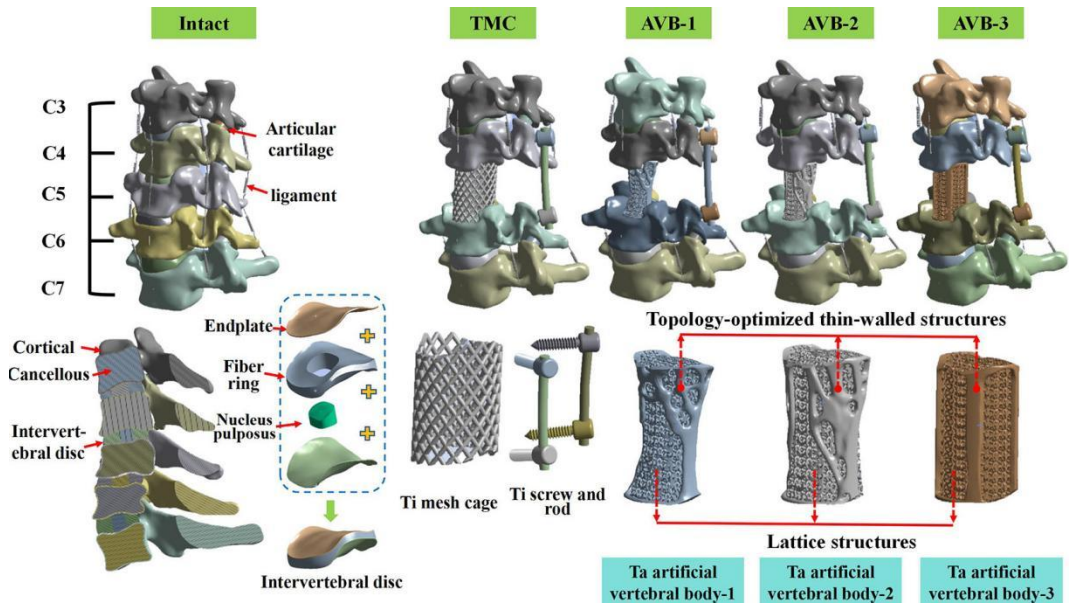


Figure 1. Intact C3-C7 cervical spine model and the model after total en bloc spondylectomy. Abbreviations: TMC: Titanium mesh cage; AVB: Artificial vertebral body; Ti: Titanium; Ta: Tantalum.

2.2 C3-C7 model after TES surgery

Simulated TES surgery to treat cervical C5 segment tumors. The surgical procedure involved the complete removal of the C5 segment and intervertebral discs located between C4-C5 and C5-C6. A Ti mesh cage or Ta artificial vertebral body was implanted between segments C4 and C6. Posterior fixation of C4 and C6 cervical segments using Ti pedicle screws and rods. The artificial vertebral body was designed to align with the anatomical characteristics of the cervical spine. The endface of the artificial vertebral body was designed to be ellipsoidal, with a long diameter of 16 mm and a short diameter of 12.6 mm, based on the shape and dimensions of the lower surface of the C4-segment vertebra and the upper surface of the C6-segment vertebra. The artificial vertebral body was designed with a height of 24 mm based on the intervertebral height between the C4 and C6 segments.

As shown in **Figure 1**, the artificial vertebral bodies were composed of thin-walled and lattice structures. The thin-walled structure formed the overall contour of the artificial vertebral body and mainly played a load-bearing role. The interior of the thin-walled structure was filled with lattices to promote bone growth. Solid thin-walled structures can impede the migration of osteoblasts into the interior of the artificial vertebral body.

Therefore, thin-walled structures should have pores that provide channels for cell migration. This study employed a topology optimization method, specifically the solid isotropic material with penalization (SIMP) model, to enhance the load-bearing capacity of thin-walled structures containing pores. Our previous research provided a comprehensive explanation of the methodology employed in the topology optimization design. [43] Imitation saddle surface (ISS) lattice structures were used to fill the interior of the thin-walled structures. This is because of the good resistance of ISS lattices to stress shielding, as indicated in our previous studies. [42] Three artificial vertebral models, designated as AVB-1, AVB-2, and AVB-3, were developed with sidewall curvatures of 0.027, 0.014, and 0 mm^{-1}, respectively. The sidewall curvature of thin-walled structures was employed as the primary design parameter. The topological thin walls were engineered with a thickness of 1 mm, and artificial vertebral bodies were designed to possess a porosity of 70%.

In this study, a Ti mesh construct (TMC) was developed with dimensions of 1 mm for rod diameter, 14 mm for overall diameter, and 24 mm in height. This construct served as the basis for assessing the biomechanical properties of the newly developed artificial vertebral bodies, specifically AVB-1, AVB-2, and AVB-3. The posterior fixation system model consisted of pedicle screws with a diameter of 4 mm and length of 21 mm and adjustable rods with a diameter of 3.5 mm. Boolean operations were conducted on the C4 segment, artificial vertebral body, and C6 segment to ensure that the anatomical curvature of the lower surface of the C4 segment and upper surface of the C6 segment remained consistent with the curvature of the respective upper and lower end faces of the artificial vertebral body.

2.3 Boundary conditions for FEA

Motion and forces in the intact cervical spine and cervical spine after TES were simulated using ANSYS software. The ALL, PLL, LF, SSL, ISL, ITL, and CL were flexible spring ligaments. The longitudinal stiffness values of the ligaments are presented in **Table 1**. [50-52] The material properties were assigned to the cortical bone, cancellous bone, endplates, annulus fibrosus, nucleus pulposus, articular cartilage, Ti mesh cage, Ta artificial vertebral bodies, and pedicle screw rod systems. The elastic

modulus and Poisson ratio of each component are listed in **Table 2**. [53] The cortical bone, cancellous bone, and intervertebral disc were set in bonding contact. The C3-C4 articular cartilage was designated as a sliding contact with the C3 inferior articular surface and bonding contact with the C4 superior articular surface. The contact configurations for the residual articular cartilage were analogous to those observed in the C3-C4 segment. The pedicle screw rod system was established in a bonding contact with the vertebrae of the C4 and C6 segments. An axial compressive load of 73.6 N was exerted on the superior surface of the C3 vertebra to replicate the weight of the human body above the C3 segment. To simulate the movements of the cervical spine, a moment of 1.8 N·m was exerted around the X-axis for flexion extension, Y-axis for lateral bending, and Z-axis for rotation. [44] The inferior surface of the C7 vertebra was constrained. The cervical segment utilized a tetrahedral mesh type with a mesh size of 1 mm. The mesh size for both the TMC and artificial vertebral body was established at 0.1 mm. The mesh counts for the TMC, AVB-1, AVB-2, and AVB-3 cervical systems were 4.97, 5.49, 5.57, and 5.68 million, respectively.

Table 1. Ligament stiffness values (N/mm)

Segments	Ligament type						
	ALL	PLL	LF	SSL	ISL	ITL	CL
C3-C4	22.25	19.5	27	5.62	0.15	2.37	33.9
C6-C7	19.5	19.5	32.5	6.25	0.15	2.37	33.9

Abbreviations: ALL: Anterior longitudinal; PLL: Posterior longitudinal; LF: Ligamentum flavum; SSL: Supraspinal; ISL: Interspinal; ITL: Intertransverse; CL: Capsular ligaments.

Table 2. Material properties used in FEA

Component	Young's modulus (MPa)	Poisson ratio
Cortical bone	12000	0.3
Cancellous bone	450	0.2
Endplate	500	0.25
Nucleus pulposus	1	0.49

Annulus fibrosus	3.4	0.45
Articular cartilage	32.9	0.3
Ti pedicle screws and rods	114000	0.34
Ti mesh cage	114000	0.34
Ta artificial vertebral body	186000	0.35

Abbreviations: FEA: Finite element analysis; Ti: Titanium; Ta: Tantalum.

3. Results

3.1 Model validation

The total range of motion (ROM) and maximum displacement of the intact, TMC, AVB-1, AVB-2, and AVB-3 cervical spine models during different motions are shown in **Figure 2**. The intact cervical spine model exhibited the greatest total range of motion (ROM) during lateral bending and rotation, while demonstrating the least total ROM during extension, as illustrated in **Figure 2(a)**. **Figure 3** illustrates a comparative analysis of the ROM of the intact cervical spine model, spanning C3 to C7, against previously established biomechanical models across different motions. In this study, the ROM observed in the intact cervical spine model was marginally less than that reported in prior experimental and finite element research. [46, 47, 54-59] Despite this, the values remained consistent with the standard deviation reported in the existing literature. The present model added a more complete ligament system than in previous studies, which increased the constraints on model motion and resulted in a reduced ROM in the intact cervical spine model. Therefore, the three-dimensional cervical spine model created was validated in this study.

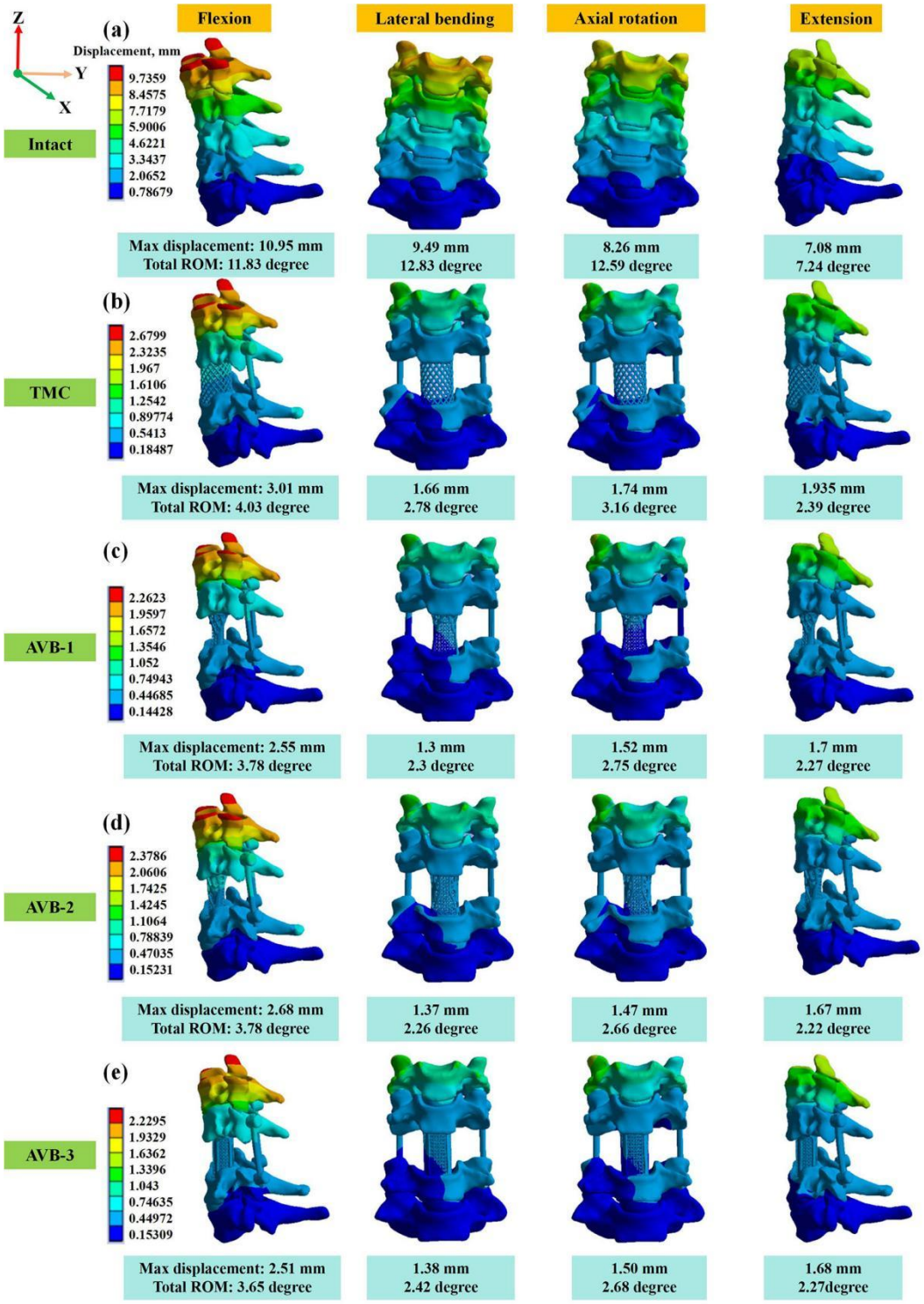


Figure 2. Total range of motion and maximum displacement of cervical spine models during different motions. (a) intact, (b) TMC, (c) AVB-1, (d) AVB-2, and (e) AVB-3 cervical spine models. Abbreviations: ROM: Range of motion; TMC: Titanium mesh cage; AVB: Artificial vertebral body.

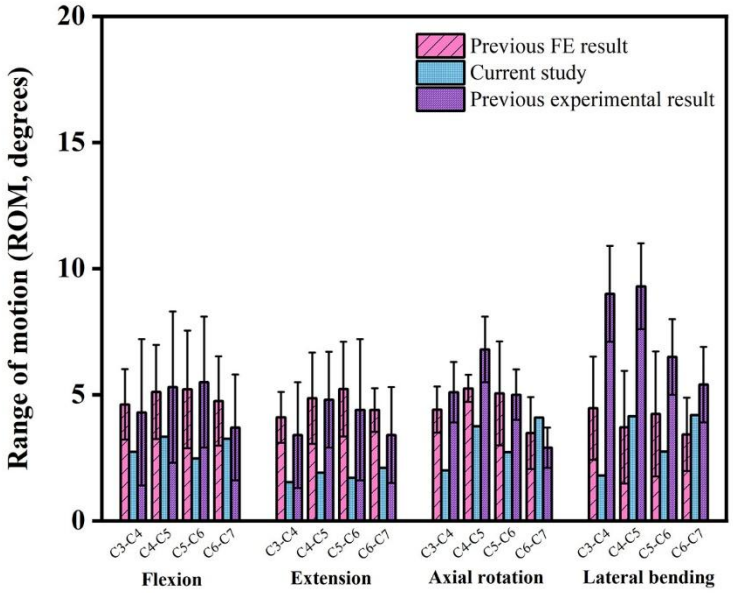


Figure 3. Comparison of range of motion of the intact cervical spine model of C3-C7 with previous biomechanical models during different motions. Abbreviations: FE: Finite element.

3.2 Range of motion (ROM)

The maximum displacements and total ROM of the cervical spine model after TES surgery with TMC, AVB-1, AVB-2, and AVB-3 in different motions are shown in **Fig. 2 (b-e)**. The maximum displacement and total ROM were significantly lower in the cervical spine model after TES surgery (TMC, AVB-1, AVB-2, and AVB-3) than in the intact model. The TMC, AVB-1, AVB-2, and AVB-3 cervical spine models showed the highest total ROM during flexion. The total ROM values in these models were similar for lateral bending, rotation, and extension. **Figure 4 (a-d)** present the ROM observed in each segment from C3 to C7 across different cervical spine models during flexion, lateral bending, rotation, and extension. The ROM of C4-C6 segments was almost zero in the TMC, AVB-1, AVB-2, and AVB-3 models. Compared with the intact model, the TMC, AVB-1, AVB-2, and AVB-3 models had significantly greater ROM between C3-C4 and significantly lower ROM between C6-C7.

The ROM percentages for the C3-C4, C4-C5, C5-C6, and C6-C7 spinal segments were determined using the following method:

$$PCT_{ROM} = \frac{ROM^*}{ROM_{total}} \times 100\% \quad (1)$$

where ROM^* is ROM between individual segments, ROM_{total} is total ROM of intact,

TMC, AVB-1, AVB-2, and AVB-3 cervical spine systems.

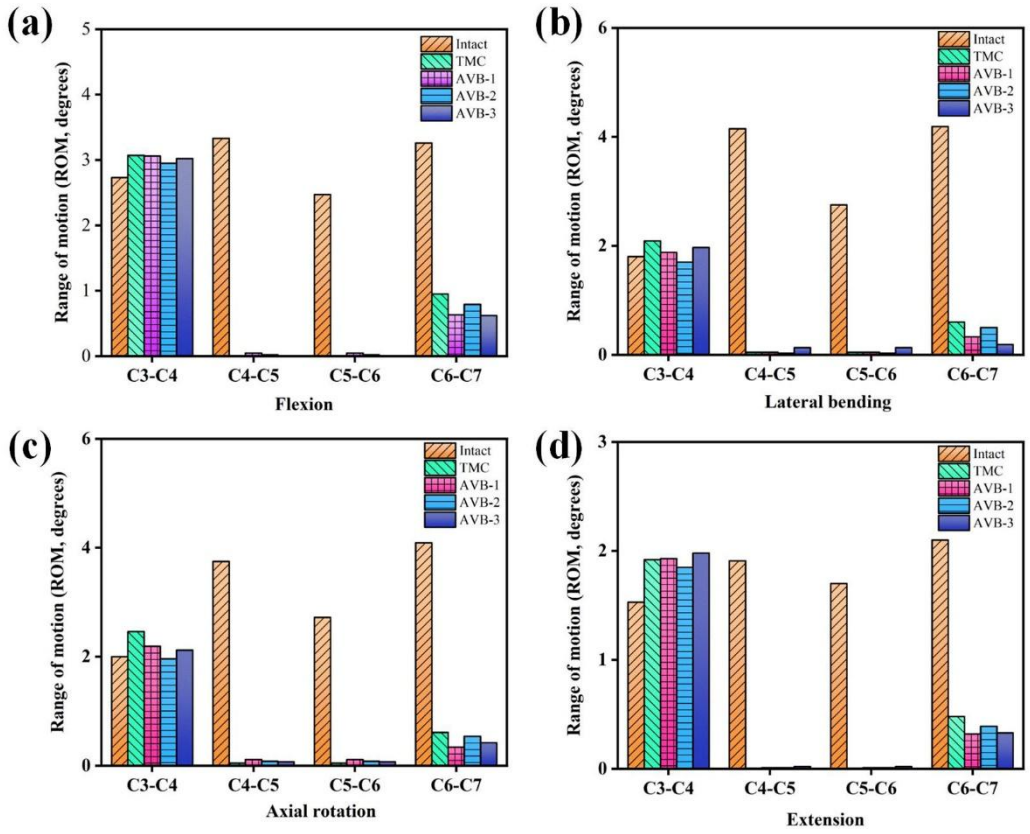


Figure 4. Range of motion between each segment of C3-C7 in different cervical spine models during different motions. (a) Flexion, (b) Lateral bending, (c) Axial rotation, and (d) Extension. Abbreviations: TMC: Titanium mesh cage; AVB: Artificial vertebral body.

The percentage of ROM between individual segments during different motions are shown in **Figure 5.** The intact model had a similar percent ROM for each cervical segment during flexion and extension. During lateral bending and rotation, the ROM percentage between the C3-C4 segments was reduced compared to the flexion-extension of the intact model. Conversely, the ROM percentage for the C4-C5 and C6-C7 segments shows an increased. The percentage of C3-C4 ROM was significantly higher in the TMC, AVB-1, AVB-2, and AVB-3 models than in the intact model, while the percentage of C6-C7 ROM was significantly lower in these models. Motion between C4-C6 in the TMC, AVB-1, AVB-2, and AVB-3 models contributed very little to the ROM of the overall cervical spine.

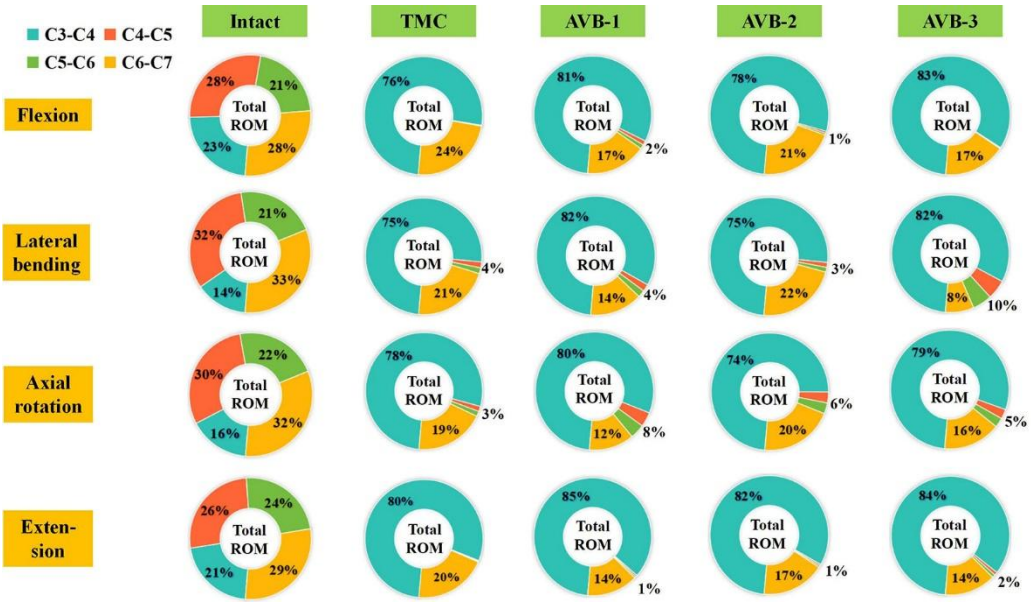


Figure 5. Percentage of ROM between individual segments in different cervical spine models during different motions. Abbreviations: ROM: Range of motion; TMC: Titanium mesh cage; AVB: Artificial vertebral body.

3.3 Stress distribution on C4 and C6 vertebrae

3.3.1 Inferior surface of the C4 vertebra

The stress distribution on the lower surface of the C4 vertebra during the different motions is shown in **Figure 6.** The intact model demonstrated a consistent distribution of stress along the lower surface of the C4 vertebra during the movements of flexion, lateral bending, rotation, and extension. In the TMC, AVB-1, AVB-2, and AVB-3 models, the inferior surface of the C4 vertebra exhibited varying levels of stress concentration. In these models, the inferior surface of the C4 vertebra experienced a notably higher average stress compared to the intact model. In the TMC, AVB-1, AVB-2, and AVB-3, flexion resulted in stress concentration on both sides of the anterior column of the C4 vertebra's inferior surface. In the context of lateral bending, stress concentrations were observed to be unilateral, specifically in the anterior and middle columns. Conversely, during rotational movements, the stress concentration was distributed in a ring pattern. In the case of extension, stress was predominantly concentrated in the middle column adjacent to the posterior column. The inferior surface of the C4 vertebra experienced a notably reduced average stress during

extension compared with flexion, lateral bending, and rotation. This decrease in stress corresponds to the alterations observed in the ROM of the cervical spine model under these specific movements.

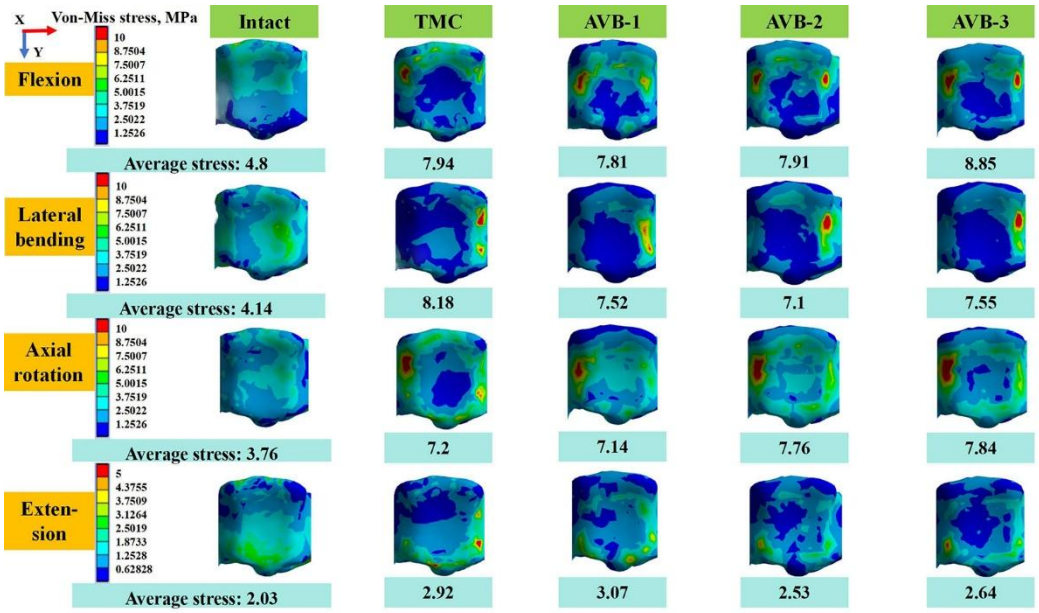


Figure 6. Stress distribution on the lower surface of C4 vertebra during different motions.

Abbreviations: TMC: Titanium mesh cage; AVB: Artificial vertebral body.

In the process of flexion, the AVB-1 model exhibited the lowest average stress on the inferior surface of C4, measuring 7.81 MPa. Conversely, the AVB-3 model demonstrated the highest average stress, reaching 8.85 MPa. During lateral bending, the stress caused by AVB-2 on the inferior surface of the C4 vertebra was 7.1 MPa, which was significantly lower than that caused by TMC (8.18 MPa). During rotation, the minimum value of the average stress on the inferior surface of the C4 vertebra is 7.14 MPa, which belongs to the AVB-1 model, whereas the maximum average stress is in the AVB-3 model (7.84 MPa). In the course of extension, the AVB-2 model exhibited the lowest average stress on the inferior surface of the C4 vertebra, measuring 2.53 MPa. Conversely, the AVB-1 model exhibited the highest average stress of 3.07 MPa.

3.3.2 Superior surface of the C6 vertebra

The stress distribution on the superior surface of C6 vertebra during different motions is shown in **Figure 7.** The intact model exhibited a uniform stress distribution on the superior surface of the C6 vertebra during all the motions. However, there were varying

degrees of stress concentration on the superior surface of the C6 vertebra for the TMC, AVB-1, AVB-2, and AVB-3 models. The area of stress concentration on the superior surface of the C6 vertebra corresponded to that on the inferior surface of the C4 vertebra.

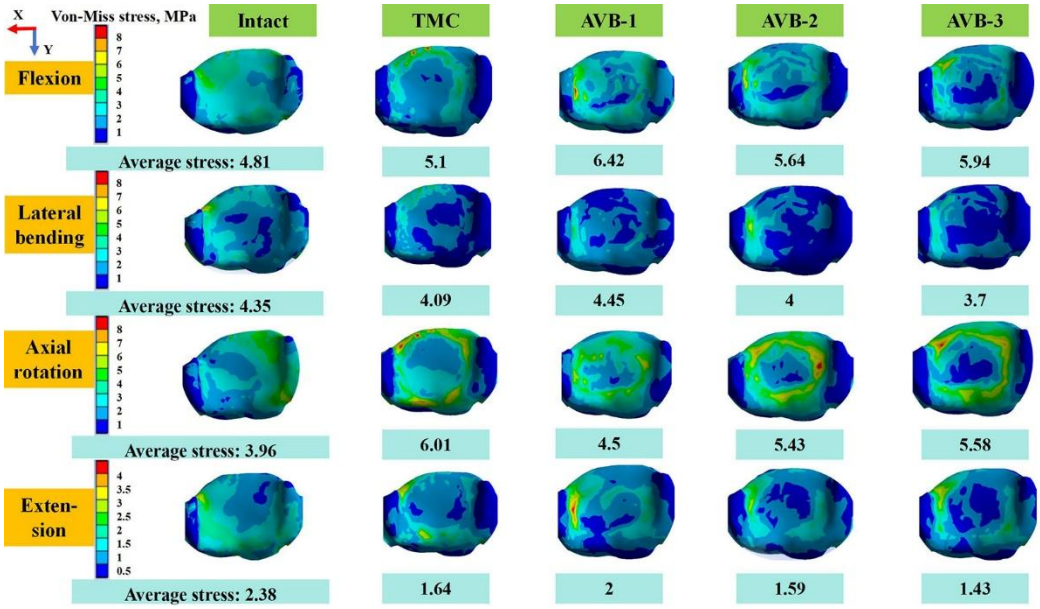


Figure 7. Stress distribution on the superior surface of C6 vertebra during different motions. Abbreviations: TMC: Titanium mesh cage; AVB: Artificial vertebral body.

In the intact model, the mean stress observed on the superior surface of C6 was comparable to that on the inferior surface of C4. In the TMC, AVB-1, AVB-2, and AVB-3 models, the average stress on the superior surface of C6 was significantly reduced compared to that on the inferior surface of C4. For example, when flexion occurred, the intact model exhibited a stress difference of 0.01 MPa between the inferior surface of C4 and the superior surface of C6. In contrast, the stress difference in the AVB-3 model reached 2.91 MPa. This was because the Ti mesh and Ta artificial vertebral body caused stress shielding of the C6 segment. The degree of stress shielding was evaluated quantitatively using the stress shielding ratio (χ).

$$\chi = 1 - \frac{\sigma_s}{\sigma_i} \quad (2)$$

where σ_i and σ_s are the average stresses on the inferior surface of the C4 and superior surface of the C6, respectively.

Figure 8 illustrates the stress shielding ratios of TMC, AVB-1, AVB-2, and AVB-3 for

various motions. During flexion, the stress shielding ratios, in increasing order, were AVB-1, AVB-2, AVB-3, and TMC. During lateral bending, the stress shielding ratios, in increasing order, were AVB-1, AVB-2, TMC, and AVB-3. During rotation, the stress shielding ratios, in increasing order, were TMC, AVB-3, AVB-2, and AVB-1. During extension, the stress shielding ratios, in increasing order, were AVB-1, AVB-2, TMC, and AVB-3.

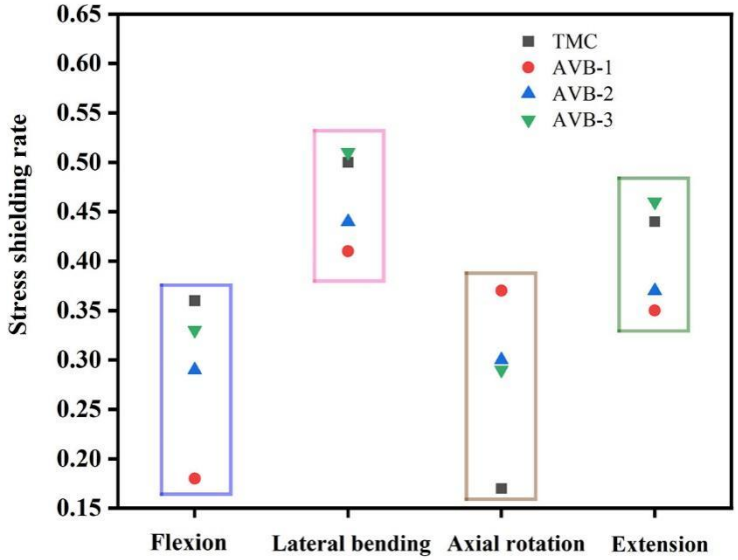


Figure 8. Stress shielding ratios of TMC, AVB-1, AVB-2, and AVB-3 during different motions.

Abbreviations: TMC: Titanium mesh cage; AVB: Artificial vertebral body

3.4 Load distribution of artificial vertebral bodies and pedicle screw rods

Figure 9 shows the stress distributions on TMC, AVB-1, AVB-2, and AVB-3. The stresses on the end faces of these components were concentrated in the regions of the interface with the cervical vertebrae. Stress concentrations on the sides of AVB-1 and AVB-2 were observed in regions where the material density varied within the topological thin-wall structure. In contrast, the stress distribution on the topological thin wall of AVB-3 was relatively uniform. The stresses in the internal lattice structures of AVB-1, AVB-2, and AVB-3 were concentrated at the strut-to-strut connection nodes, which was consistent with our previous findings. [42]

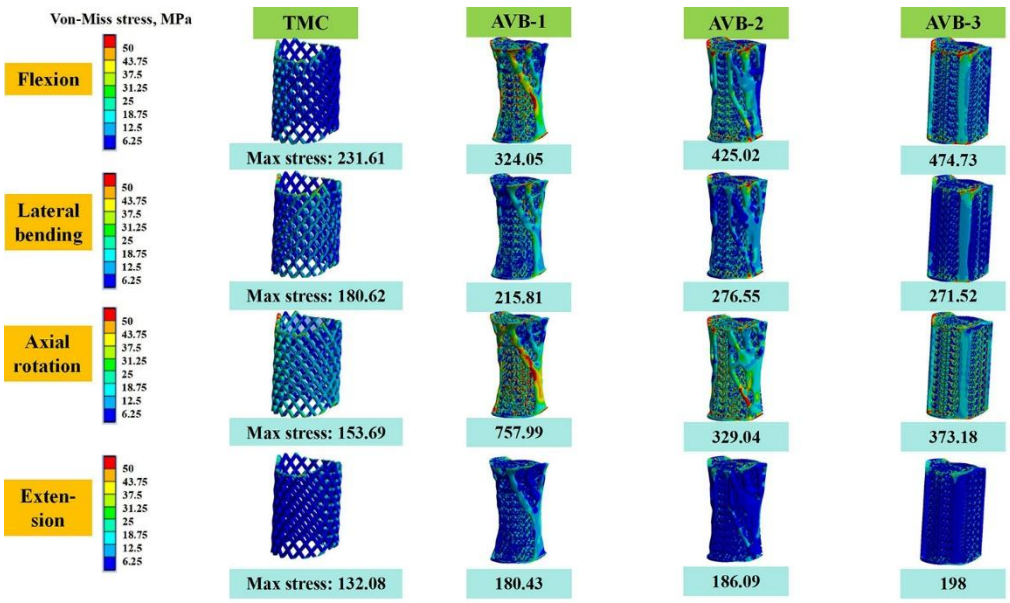


Figure 9. Stress distribution on TMC, AVB-1, AVB-2, and AVB-3 during different motions. Abbreviations: TMC: Titanium mesh cage; AVB: Artificial vertebral body.

The stress distribution on the pedicle screw rod fixation system is shown in **Figure 10.** Stresses were concentrated in the head of the screws and in the region where the screw caps attached to the adjusting rods, which can be attributed to that it was in this region that the pedicle screw rods were subjected to the greatest bending moment.

During flexion, the maximum stress values of 499.41 MPa and 469.37 MPa on the pedicle screw rods of TMC and AVB-1 cervical spine systems, respectively, were significantly higher than those on the TMC and the AVB-1 (231.61 MPa and 324.05 MPa, respectively). The findings suggest that during flexion, the load is primarily transmitted via the pedicle screw rods in both the TMC and AVB-1 cervical spine systems. The maximum stress values on the AVB-2 and AVB-3 were 425.02 MPa and 474.73 MPa in the AVB-2 and AVB-3 cervical spine systems, respectively, which were significantly higher than the maximum stresses on the corresponding pedicle screw rods (277 MPa and 266.54 MPa, respectively), suggesting that the loads were mainly transmitted through the artificial vertebral body (AVB-2 and AVB-3). In a similar manner, the principal pathways for force transmission in the TMC, AVB-1, AVB-2, and AVB-3 cervical spine systems can be identified during lateral bending, rotation, and extension movements.

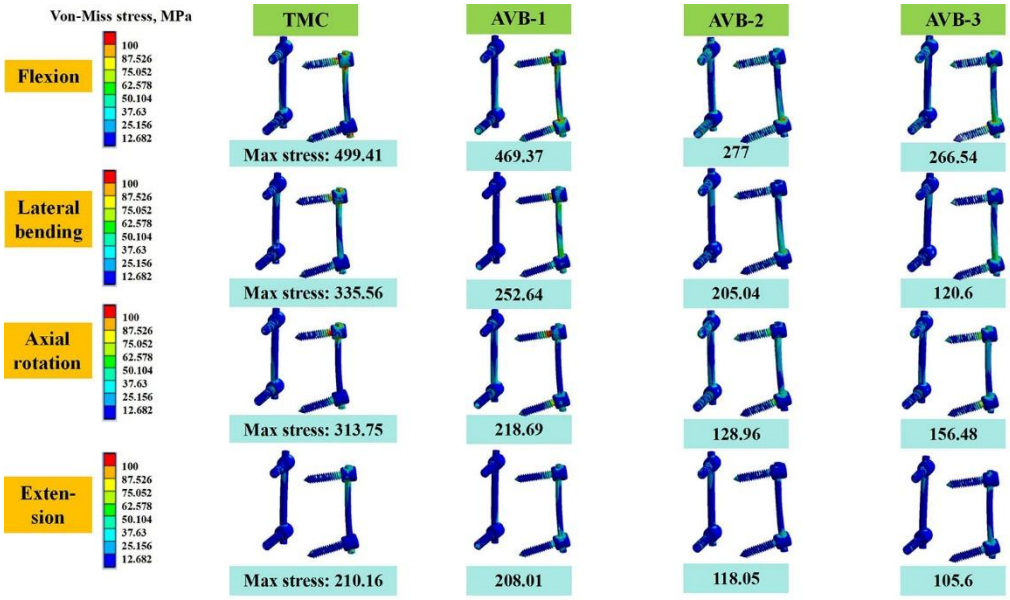


Figure 10. Stress distribution on pedicle screw rod fixation system during different motions. Abbreviations: TMC: Titanium mesh cage; AVB: Artificial vertebral body.

The percentage of stress on the TMC, AVB-1, AVB-2, AVB-3, and pedicle screw rods can be calculated as follows:

$$PCT_{stress} = \frac{Stress^{*}}{Stress_{total}} \times 100\% \quad (3)$$

where $Stress^{*}$ is the stress on the TMC, AVB-1, AVB-2, AVB-3, and pedicle screw rods, $Stress_{total}$ is the sum of the stresses on the artificial vertebral body and pedicle screw rods.

The percentages of stress on the TMC, AVB-1, AVB-2, AVB-3, and pedicle screw rods are shown in **Figure 11.** The PCT_{stress} was used to determine the main load-bearing component of the fused segment under different motions. For example, during flexion, the PCT_{stress} of the pedicle screw rods in the TMC cervical spine system was 68%, which was twice that of the TMC. Therefore, pedicle screw rods play a major load-bearing role in this system. Similarly, the main load-bearing component in the AVB-1 cervical spine system was the pedicle screw rod, the main load-bearing component in the AVB-2 cervical spine system was AVB-2, and the main load-bearing component in the AVB-3 cervical spine system was AVB-3. Similarly, the primary load-bearing components of various cervical spine systems can be identified for alternative motions.

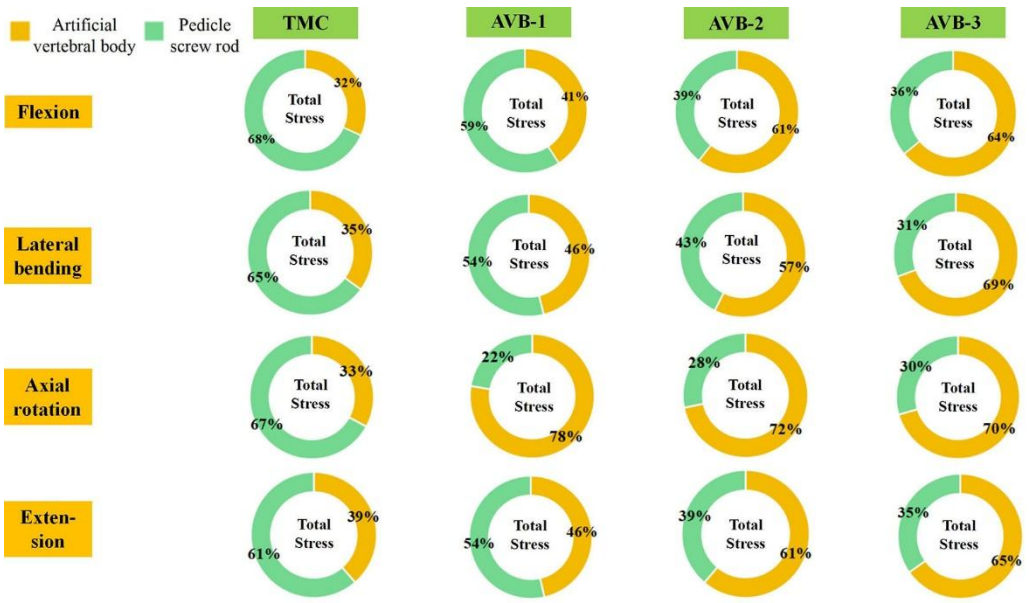


Figure 11. Percentages of stress on TMC, AVB-1, AVB-2, AVB-3, and pedicle screw rods during different motions. Abbreviations: TMC: Titanium mesh cage; AVB: Artificial vertebral body.

3.5 Strain energy ration of C3-C4 and C6-C7 disc

Strain energy is the potential energy stored in the form of stress and strain during the deformation of an object under a force. The effect of the Ti mesh, Ta artificial vertebral body, and pedicle screw rods on adjacent intervertebral discs can be quantitatively analyzed by comparing the strain energy of the intervertebral disc as a proportion of the total strain energy of the cervical spine system (strain energy ratio, η). The strain energy ratio was calculated as follows:

$$\eta = \frac{U_i}{U_T} \quad (4)$$

where U_i is strain energy of the intervertebral disc, U_T is the strain energy of the cervical spine system.

The total strain energies of the intact, TMC, AVB-1, AVB-2, and AVB-3 cervical spine systems are presented in **Table 3**. The total strain energy observed in the intact cervical spine system was markedly greater than that in the TMC, AVB-1, AVB-2, and AVB-3 systems for all motion types.

Table 3. Total strain energies of the intact, TMC, AVB-1, AVB-2, and AVB-3 cervical spine systems during different motions (mJ)

Motions	Intact	TMC	AVB-1	AVB-2	AVB-3
Flexion	136.76	60.68	55.78	52.05	50.55
Lateral bending	124.04	31.61	26.37	24.14	27.88
Axial rotation	121.66	41.77	37.16	33.05	32.81
Extension	47.97	23.08	21.65	19.88	20.8

Abbreviations: TMC: Titanium mesh cage; AVB: Artificial vertebral body.

The strain energy ratios of the C3-C4 disc in the intact, TMC, AVB-1, AVB-2, and AVB-3 cervical spine systems are illustrated in **Figure 12**. The strain energy ratio of the C3-C4 disc in the intact cervical spine system was significantly lower than that of the C3-C4 disc in the TMC, AVB-1, AVB-2, and AVB-3 cervical spine systems during all motions. For example, when flexion occurred, the strain energy ratios for the C3-C4 disc in the TMC, AVB-1, AVB-2, and AVB-3 cervical spine systems were 0.41, 0.46, 0.44, and 0.46, respectively. These values were double the strain energy ratio of the C3-C4 disc in the intact cervical spine system (0.2). The findings suggest that the C3-C4 disc exhibited greater involvement in the deformation of the cervical spine following the implantation of the Ti mesh, Ta artificial vertebral body, and pedicle screw rods.

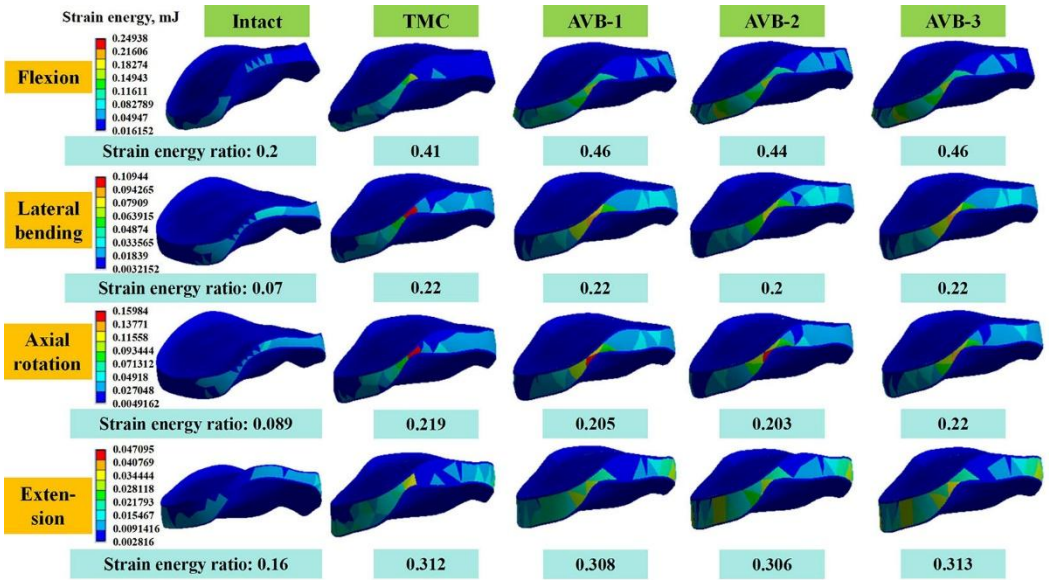


Figure 12. Strain energy ratio of the C3-C4 disc in the intact, TMC, AVB-1, AVB-2, and AVB-3

cervical spine systems during different motions. Abbreviations: TMC: Titanium mesh cage; AVB: Artificial vertebral body.

The strain energy ratios of the C6-C7 disc in the intact, TMC, AVB-1, AVB-2, and AVB-3 cervical spine systems are shown in **Figure 13.** Compared with the intact cervical spine system, the strain-energy ratios of the C6-C7 discs in the TMC, AVB-1, AVB-2, and AVB-3 cervical spine systems were significantly reduced during all motions. For example, during extension, the strain energy ratio of C6-C7 discs in the intact cervical system was 0.114, which was significantly higher than that of C6-C7 discs in the TMC, AVB-1, AVB-2, and AVB-3 cervical spine systems (0.072, 0.068, 0.069, and 0.076, respectively). In the cervical spine, the implantation of the Ti mesh, Ta artificial vertebral body, and pedicle screw rods resulted in a notable decrease in the deformation of the C6-C7 disc, unlike that of the C3-C4 disc.

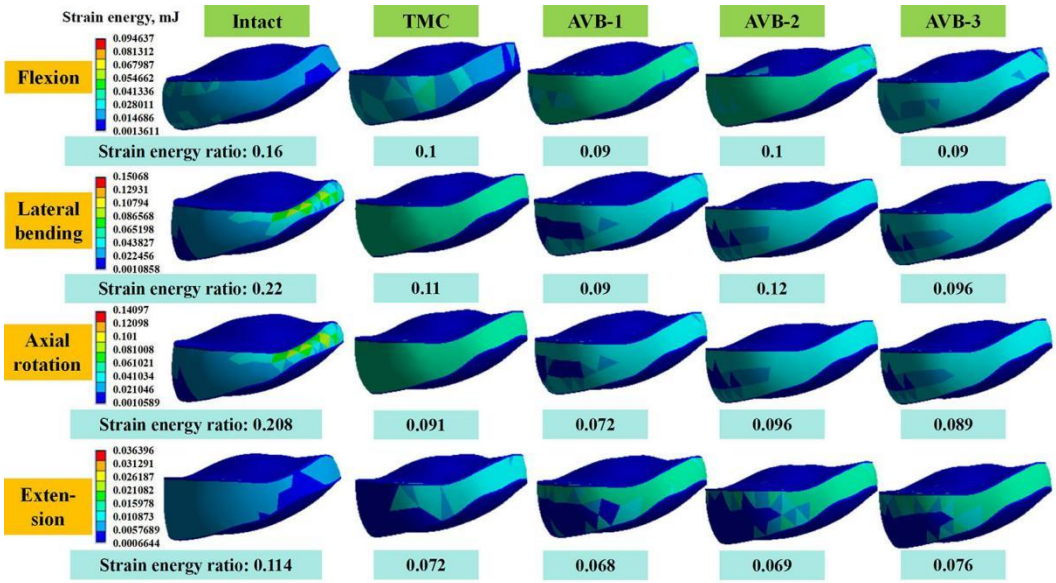


Figure 13. Strain energy ratio of the C6-C7 disc in the intact, TMC, AVB-1, AVB-2, and AVB-3 cervical spine systems during different motions. Abbreviations: TMC: Titanium mesh cage; AVB: Artificial vertebral body.

3.6 Strain energy ration of C3-C4 and C6-C7 articular cartilage

The strain energy ratios of the C3-C4 articular cartilage in the intact, TMC, AVB-1, AVB-2, and AVB-3 cervical spine systems are illustrated in **Figure 14.** A significantly

higher strain energy ratio of the C3-C4 articular cartilage was observed in the TMC, AVB-1, AVB-2, and AVB-3 cervical spine systems than in the intact cervical spine system during all motions. For example, during rotation, the strain energy ratio of the C3-C4 articular cartilage in the intact cervical spine system was 0.057, which was significantly lower than that of the C3-C4 articular cartilage in the TMC, AVB-1, AVB-2, and AVB-3 systems (0.41, 0.41, 0.38, and 0.38, respectively). This indicated that implantation of the Ti mesh, Ta artificial vertebral body, and pedicle screw rods caused increased deformation of the C3-C4 articular cartilage.

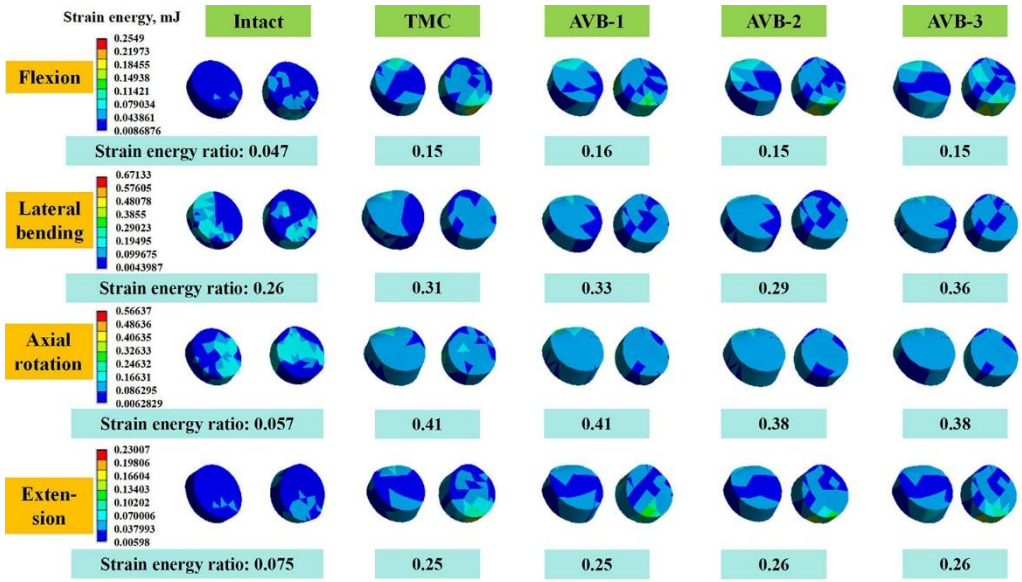


Figure 14. Strain energy ratios of the C3-C4 articular cartilage in the intact, TMC, AVB-1, AVB-2, and AVB-3 cervical spine systems during different motions. Abbreviations: TMC: Titanium mesh cage; AVB: Artificial vertebral body.

The strain energy ratios of the C6-C7 articular cartilage in the intact, TMC, AVB-1, AVB-2, and AVB-3 cervical spine systems are illustrated in **Figure 15.** Decreased strain energy ratios of C6-C7 articular cartilage in the TMC, AVB-1, AVB-2, and AVB-3 cervical spine systems compared to the intact cervical spine system during all motions. For example, during rotation, the strain energy ratios of the C6-C7 articular cartilage in the TMC, AVB-1, AVB-2, and AVB-3 cervical spine systems were 0.018, 0.015, 0.03, and 0.019, respectively, which were lower than those of the C6-C7 articular cartilage in the intact cervical spine system (0.071). Therefore, implantation of the Ti mesh, Ta

artificial vertebral body, and pedicle screw rods decreased the deformation of the C6-C7 articular cartilage.

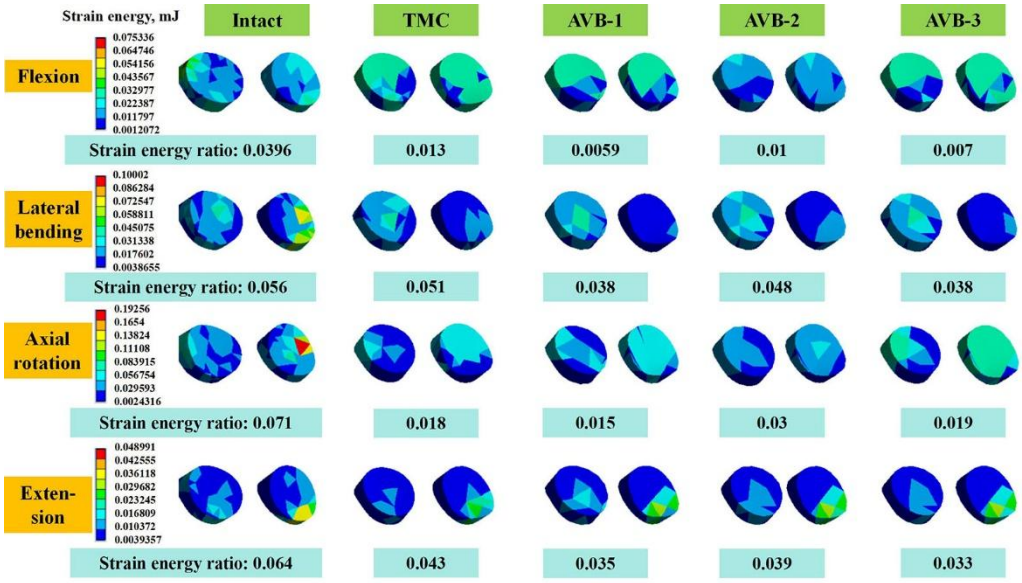


Figure 15. Strain energy ratios of the C6-C7 articular cartilage in the intact, TMC, AVB-1, AVB-2, and AVB-3 cervical spine systems during different motions. Abbreviations: TMC: Titanium mesh cage; AVB: Artificial vertebral body.

4. Discussion

To treat cervical spine tumors, TES surgery was required to completely remove the diseased vertebrae (e.g., C5 segment) and implant an artificial vertebral body and posterior fixation to restore intervertebral height and load bearing of the neck region. The mechanical property disparities between Ti mesh, Ta artificial vertebral bodies, and Ti pedicle screw rods, in comparison to human vertebral bone, substantially influence cervical spine motion and the forces exerted upon it. The incorporation of Ti mesh, Ta artificial vertebral bodies, and titanium pedicle screw rods into the cervical spine significantly enhanced its stiffness. This enhancement resulted in a marked decrease in both the maximum displacement and ROM within the TES model (TMC, AVB-1, AVB-2, and AVB-3) compared to the intact model under equivalent loading conditions, as depicted in **Figure 2**. The fixation effect of the Ti mesh, Ta artificial vertebral bodies, and pedicle screw rods limited the motion of the C4 and C6 segments, resulting in an almost zero C4-C6 ROM, as shown in **Figure 4**. In order to achieve motion

compensation, the TES model exhibited a notable increase in the percentage of ROM between the C3-C4 segments when compared to the intact model, as depicted in **Figure 5**.

As shown in **Figure 1**, the fused segments composed of Ti mesh, Ta artificial vertebral bodies, pedicle screw rods, and C4 and C6 vertebral bodies had significantly higher stiffness than the adjacent segments. This fusion obstructed the downward transmission of loads, thereby establishing a stress shield for the C6-C7 disc and C7 vertebral body. Consequently, the ROM of the C6-C7 segments in the TES model was reduced compared to that in the intact model (Figure 4).

The percentage of ROM between C3-C4, C4-C5, C5-C6, and C6-C7 segments shows the effect of Ti mesh, Ta artificial vertebral body, and fixation systems on cervical ROM. For example, as shown in **Figure 5**, during rotation, the immobilization of Ti mesh, Ta artificial vertebral bodies, and pedicle screw rods caused the percentage of ROM between C4-C6 to decrease from 52% in the intact model to 3%, 8%, 6%, and 5% in the TMC, AVB-1, AVB-2, and AVB-3 models, respectively. After C4 and C6 segments were fixed to form a fused segment, the stiffness increased significantly. Under external loading, the significantly lower stiffness of the C3-C4 segments compared with the fused segments resulted in the C3-C4 segments contributing to higher mobility. The percentage of ROM of C3-C4 increased from 16% in the intact model to 78%, 80%, 74%, and 79% in the TMC, AVB-1, AVB-2, and AVB-3 models, respectively. The high stiffness of the fused segments produces stress shielding, which reduces the load distribution on the C6-C7 segments, resulting in a reduced percentage of ROM of C6-C7. The percentage of ROM of C6-C7 decreased from 32% in the intact model to 19%, 12%, 20%, and 16% in the TMC, AVB-1, AVB-2, and AVB-3 models, respectively.

The average stress on the inferior surface of the C4 vertebral body depended on the load distribution, stiffness, and contact area with the C4 segment of the Ti mesh, Ta artificial vertebral bodies, and pedicle screw rods. The cervical C4 and C6 vertebral bodies shared forces and moments with the Ti mesh, Ta artificial vertebral bodies, and pedicle screw rods. The implants (Ti mesh and Ta artificial vertebral bodies) and fixation system (pedicle screw rods) were connected in parallel. Based on the percentage of

stress on the TMC, AVB-1, AVB-2, AVB-3, and pedicle screw rods, it was possible to determine the main load-bearing components under different motions. In the pedicle screw rod system and artificial vertebral bodies, the component with the highest stress percentage was the primary load-bearing component. As shown in **Figure 11**, during flexion, the main load-bearing components of the Ti mesh, AVB-1, AVB-2, and AVB-3 cervical spine systems were pedicle screw rods, pedicle screw rods, AVB-2, and AVB-3, respectively. During lateral bending, the main load-bearing components of the TMC, AVB-1, AVB-2, and AVB-3 cervical spine systems were pedicle screw rods, pedicle screw rods, AVB-2, and AVB-3, respectively. During rotation, the main load-bearing components of the TMC, AVB-1, AVB-2, and AVB-3 cervical spine systems were pedicle screw rods, AVB-1, AVB-2, and AVB-3, respectively. During extension, the main load-bearing components of the TMC, AVB-1, AVB-2, and AVB-3 cervical spine systems were pedicle screw rods, pedicle screw rods, AVB-2, and AVB-3, respectively. When the pedicle screw rods were the primary load-bearing components, the higher stress on the pedicle screw rods indicated a higher loading of the fused segment, which resulted in a higher average stress on the lower surface of the C4 vertebral body. For example, during lateral bending, the primary load-bearing components of both the TMC and AVB-1 cervical spine systems were the pedicle screw rods. **Figures 9** and **10** illustrate that the maximum stress experienced by the pedicle screw rods in the TMC cervical spine system reached 335.56 MPa. This value is notably higher compared to the AVB-1 cervical spine system, which recorded a maximum stress of 252.64 MPa. Therefore, the average stress on the inferior surface of C4 in the TMC cervical spine system was higher than that in the AVB-1 cervical spine system (**Figure 6**).

When the Ta synthetic vertebral implant served as the primary load-bearing component, an increase in the percentage of stress on the artificial vertebral body corresponded to an increase in its stiffness. The average stress on the inferior surface of the C4 vertebra increased as the stiffness of the artificial vertebral body was augmented. For instance, during lateral bending, the primary load-carrying elements of the AVB-2 and AVB-3 cervical spine systems were the AVB-2 and AVB-3, respectively. As shown in **Figure 11**, the percentage of stress in AVB-2 was 57%, which was lower than that in AVB-3

(69%). This indicated that the stiffness of AVB-2 was lower than that of AVB-3. Therefore, the average stress on the inferior surface of C4 in the AVB-3 cervical spine system was higher than that in the AVB-2 cervical spine system (**Figure 6**).

Because the stiffness of the Ti mesh, artificial vertebral bodies, and pedicle screw rods was much higher than that of the vertebral bone, the transfer of load from C4 to C6 was obscured by the Ti mesh, artificial vertebral bodies, and pedicle screw rods. Consequently, the average stress on the superior surface of C6 was significantly reduced compared to the inferior surface of C4 in the TMC, AVB-1, AVB-2, and AVB-3 systems, as illustrated in **Figures 6** and **7**. Stiffness of the artificial vertebral bodies and pedicle screw rods during different motions was an important factor affecting the stress shielding ratio. Loads tend to be transferred to the structure along paths of greater stiffness. Therefore, the stiffness of artificial vertebral bodies and pedicle screw rods can be evaluated based on their percentage of stress. The higher percentage of stress on the artificial vertebral bodies and pedicle screw rods indicated their higher stiffness, which resulted in a greater degree of stress shielding of the C6 superior surface. For example, as shown in **Figure 11**, during flexion, the percentage of stress on the pedicle screw rods in the TMC cervical spine system was 68%, which was higher than that on AVB-3 (64%), AVB-2 (60%), and the pedicle screw rods in the AVB-1 cervical spine system (59%). Therefore, the stress shielding ratio was higher in the TMC cervical spine system than that in the AVB-1, AVB-2, and AVB-3 cervical spine systems during flexion (**Figure 8**).

Throughout all movements, the pedicle screw rods served as the principal load-bearing elements in the TMC cervical spine system, indicating that the titanium mesh possessed inadequate load-bearing capacity. With the exception of rotation, the primary load-bearing components of the AVB-1 cervical spine system were pedicle screw rods, suggesting that the load-bearing capacity of AVB-1 was limited during flexion, lateral bending, and extension. During rotation, the torsional stiffness of the pedicle screw rods was lower than that of AVB-1, owing the lack of constraints from the horizontal adjusting rods. Therefore, during rotation, AVB-1 became the primary load-bearing component of the AVB-1 cervical spine system. During all motions, the primary load-

bearing components of the AVB-2 and AVB-3 cervical spine systems were artificial vertebral bodies, indicating that AVB-2 and AVB-3 could meet the load-bearing demands for clinical applications. The clinical expectation is that the artificial vertebral body will perform the primary load-bearing function, whereas the pedicle screw rods will primarily serve as fixation. If too much load is transmitted to the pedicle screw rods, it can cause them to loosen and increase the risk of failure. The Ti mesh and AVB-1 had difficulty providing long-term stability for cervical fusion because of their insufficient stiffness and excessive loads were transferred to the pedicle screw rods.

The patient's diseased C5 segment and attached disc were completely removed by TES surgery. Following the implantation of the artificial vertebral body and pedicle screw rods, there was a marked increase in stiffness of the cervical fusion segment. This alteration in stiffness likely exerts a negative impact on the adjacent intervertebral discs at C3-C4 and C6-C7. As shown in **Figure 12**, the strain-energy ratio of the C3-C4 disc in the intact cervical spine system was significantly lower than that of the C3-C4 disc in the TMC, AVB-1, AVB-2, and AVB-3 cervical spine systems during all motions. This is due to the fact that the deformation and ROM of the C4-C6 fusion segment is almost zero after implantation of the Ti mesh, artificial vertebral body, and pedicle screw rods (**Figures 4 and 5**). The C4-C5 and C5-C6 discs were completely removed, and the contribution of the C3-C4 disc to the total strain of the cervical spine system was increased to compensate for the deformation of the C4-C5 and C5-C6 discs under the same load. Therefore, implantation of Ti mesh, artificial vertebral bodies, and pedicle screw rods increases the risk of overstrain of the C3-C4 intervertebral discs and tends to trigger degenerative lesions in the C3-C4 intervertebral discs.

Figure 13 illustrates that, in comparison to the intact cervical spine system, the strain energy ratios of the C6-C7 discs in the TMC, AVB-1, AVB-2, and AVB-3 cervical spine systems were significantly diminished across all motions. This is because implantation of the Ti mesh, artificial vertebral bodies, and pedicle screw rods significantly increased the stiffness of the C4-C6 fusion segment. The fusion segment produced stress shielding on the C6-C7 disc, resulting in reduced stress and strain in the C6-C7 disc. The stress-shielding effect caused by the fusion of segments reduces stress stimulation in the C6-

C7 intervertebral disc, thereby increasing the likelihood of degenerative disc disease in this region.

Figures 4 and 5 demonstrate that the C3-C4 ROM was markedly increased in the cervical spine system incorporating titanium mesh and an artificial vertebral body, as opposed to the intact cervical spine system. This augmentation in ROM leads to an increase in the strain-energy ratios within the C3-C4 articular cartilage, as illustrated in **Figure 14**. After TES, the patient lost the C4-C5 and C5-C6 articular cartilages. To compensate for the overall ROM of the cervical spine under the same load, the C3-C4 articular cartilages was excessively involved in deformation of the cervical system. This increases the risk of degenerative diseases of the C3-C4 articular cartilage due to overstrain. However, as shown in **Figure 15**, the strain energy ratios of the C6-C7 articular cartilage in the TMC, AVB-1, AVB-2, and AVB-3 cervical spine systems were lower than in those the intact cervical spine system during all motions. This was because the high-stiffness fusion segment produced stress shielding on the C6-C7 segment, which reduced the ROM of the C6-C7 segments (**Figures 4 and 5**). This results in the C6-C7 articular cartilage not being stimulated by normal stresses and strains and is prone to degenerative cartilage disease.

In summary, to reduce the stress-shielding effect on adjacent cervical segments, an artificial vertebral body should have a good load bearing-capacity with low stiffness. TMC and AVB-1 demonstrated good resistance to stress shielding in all motions but were unable to provide long-term stability for cervical fusion because of their insufficient load-bearing capacity. AVB-3 was able to share most of the load for the pedicle screw rods; however, the stress shielding effect was significant owing to the higher stiffness. AVB-2 had a good load-bearing capacity and moderate stiffness under all motions. This helps reduce the load distribution of the pedicle screw rods and provides long-term stability for cervical fusion. Simultaneously, AVB-2 significantly reduced the stress-masking effect on the adjacent segments compared to AVB-3. Therefore, AVB-2 is the optimal artificial vertebral body design option with the potential for clinical application.

5. Conclusions

This study involved the development of cervical spine models under both intact and post-TES conditions. Finite element analysis was employed to investigate the effects of titanium mesh, artificial vertebral bodies, and pedicle screw rods on the ROM, contacting vertebrae, adjacent intervertebral discs, and the articular cartilage. Load transfer patterns between the artificial vertebral bodies and pedicle screw rods were analyzed. The conclusions are as follows.

Following the implantation of the TMC, AVBs, and pedicle screw rods, the postoperative cervical spine model exhibited a significantly reduced maximum displacement and ROM compared to the intact cervical spine model when subjected to identical loads and moments. The percentage of C3-C4 ROM was significantly higher in the TMC, AVB-1, AVB-2, and AVB-3 models than in the intact model, while the percentage of C6-C7 ROM was significantly lower in these models. Motion between C4-C6 in the TMC, AVB-1, AVB-2, and AVB-3 models contributed very little to the ROM of the overall cervical spine.

In the TMC, AVB-1, AVB-2, and AVB-3 models, the mean stress on the inferior surface of the C4 vertebra was significantly greater than that in the intact model. In the intact model, the mean stress on the superior surface of the C6 vertebra was comparable to that on the inferior surface of the C4 vertebra. However, there was a significant reduction in the average stress on the superior surface of C6 compared with the inferior surface of C4 in the TMC, AVB-1, AVB-2, and AVB-3 models.

During flexion, the stress shielding ratios in increasing order were AVB-1, AVB-2, AVB-3, and TMC. During lateral bending, the stress shielding ratios in increasing order were AVB-1, AVB-2, TMC, and AVB-3. During rotation, the stress shielding ratios in increasing order were TMC, AVB-3, AVB-2, and AVB-1. During extension, the stress shielding ratios in increasing order were AVB-1, AVB-2, TMC, and AVB-3.

The strain energy ratios of the C3-C4 intervertebral disc and articular cartilage in the TMC and AVBs systems were notably greater than those observed in the intact cervical spine model. This suggests that the C3-C4 intervertebral disc and articular cartilage have a high risk of overstrain and are susceptible to induced degenerative disease after implantation of Ti mesh, artificial vertebral bodies, and pedicle screw rods. The strain

energy ratios of the C6-C7 intervertebral discs and articular cartilage in the TMC and AVBs systems were notably lower compared to those in the intact cervical spine model. This finding suggests that the C6-C7 intervertebral discs and articular cartilage are prone to degeneration owing to the absence of normal stress-strain stimulation following the implantation of the Ti mesh, artificial vertebral bodies, and pedicle screw rods.

In the TMC and AVB-1 systems, the pedicle screw rods had a high percentage of stress and played a primary load-bearing role. In the AVB-2 and AVB-3 systems, the loads were primarily transferred to the artificial vertebral bodies, which played a primary load-bearing role. It was difficult for TMC and AVB-1 to provide long-term stability for cervical fusion because of insufficient stiffness and excessive load transfer to pedicle screw rods. The stress-shielding effect of AVB-3 was significant owing to its high stiffness. The AVB-2 demonstrated substantial load-bearing capacity and moderate stiffness across all movements. This characteristic contributes to diminishing the load distribution on the pedicle screw rods, thereby ensuring long-term stability in cervical fusion procedures. Simultaneously, AVB-2 significantly reduced the stress-masking effect on the adjacent segments compared to AVB-3. Therefore, AVB-2 is the optimal artificial vertebral body design option with potential for clinical application.

Declarations

Ethics approval and consent to participate

This study was approved by the Medical Ethics Committee of the General Hospital of the Xinjiang Military Region of the People's Liberation Army and complied with the Declaration of Helsinki. The data used were obtained from healthy volunteers who provided informed consent or from anonymized clinical imaging databases. The study did not involve any interventions on living human subjects or the disclosure of personal privacy information; thus, it met the criteria for exemption from informed consent.

Consent for publication

Not applicable.

Availability of data and materials

The datasets used and/or analysed during the current study are available from the corresponding author on reasonable request.

Competing interests

The authors declare that they have no competing interests.

Funding

This research was funded by [Natural Science Foundation of Xinjiang Uygur Autonomous Region, China], grant number [2023D01A86]; ["Mount Tianshan Talent" High-level Talent Program in Medicine and Health, Xinjiang Uygur Autonomous Region, China], grant number [TSYC202401A031]; [Key R&D plan project of Xinjiang Uygur Autonomous Region, China], grant number [2025B03006-1].

Authors' contributions

Yutao Zhang: Investigation, Methodology, Writing-Original draft, Validation. Wurikaixi Aiyiti: Methodology, Conceptualization, Writing-review & Editing. Jintao Li: Investigation. Yong Teng: Methodology, Conceptualization. All authors read and approved the final manuscript.

Acknowledgments

Not applicable.

References

1. Shimizu T, Kato S, Yokogawa N, et al. Total en bloc spondylectomy for primary tumors of the thoracic and lumbar spine: A review article. *Seminars in Spine Surgery* 2024; 36: 101137. https://doi.org/10.1016/j.semss.2024.101137.

2. Wang B, Liu M, Ke W, et al. Finite element analysis of additive manufactured porous peek artificial vertebral bodies in lumbar total en bloc spondylectomy. *The Spine Journal* 2025; 25: 1042-1049. https://doi.org/10.1016/j.spinee.2024.10.026.

3. Jang J-W, Lee J-K, Lee J-H, et al. Effect of posterior subsidence on cervical alignment after anterior cervical corpectomy and reconstruction using titanium mesh cages in degenerative cervical disease. *Journal of Clinical Neuroscience* 2014; 21: 1779-1785. https://doi.org/10.1016/j.jocn.2014.02.016.

4. Hu B, Wang L, Song Y, et al. A comparison of long-term outcomes of

nanohydroxyapatite/polyamide-66 cage and titanium mesh cage in anterior cervical corpectomy and fusion: A clinical follow-up study of least 8 years. *Clinical Neurology and Neurosurgery* 2019; 176: 25-29. https://doi.org/10.1016/j.clineuro.2018.11.015.

5. Chen Y, Chen D, Guo Y, et al. Subsidence of Titanium Mesh Cage: A Study Based on 300 Cases. *Clinical Spine Surgery* 2008; 21.

6. Zhang Y-W, Deng L, Zhang X-X, et al. Three-Dimensional Printing-Assisted Cervical Anterior Bilateral Pedicle Screw Fixation of Artificial Vertebral Body for Cervical Tuberculosis. *World Neurosurgery* 2019; 127: 25-30. https://doi.org/10.1016/j.wneu.2019.03.238.

7. Cao Y, Yang N, Wang S, et al. The application of 3D-printed auto-stable artificial vertebral body in en bloc resection and reconstruction of thoracolumbar metastases. *Journal of Orthopaedic Surgery and Research* 2023; 18: 638. https://doi.org/10.1186/s13018-023-04135-3.

8. Chung KS, Shin DA, Kim KN, et al. Vertebral Reconstruction with Customized 3-Dimensional−Printed Spine Implant Replacing Large Vertebral Defect with 3-Year Follow-up. *World Neurosurgery* 2019; 126: 90-95. https://doi.org/10.1016/j.wneu.2019.02.020.

9. Liebsch C, Aleinikov V, Kerimbayev T, et al. In vitro comparison of personalized 3D printed versus standard expandable titanium vertebral body replacement implants in the mid-thoracic spine using entire rib cage specimens. *Clinical Biomechanics* 2020; 78: 105070. https://doi.org/10.1016/j.clinbiomech.2020.105070.

10. Kang J, Dong E, Li X, et al. Topological design and biomechanical evaluation for 3D printed multi-segment artificial vertebral implants. *Materials Science and Engineering: C* 2021; 127: 112250. https://doi.org/10.1016/j.msec.2021.112250.

11. Abd-Elaziem W, Darwish MA, Hamada A, et al. Titanium-Based alloys and composites for orthopedic implants Applications: A comprehensive review. *Materials & Design* 2024; 241: 112850. https://doi.org/10.1016/j.matdes.2024.112850.

12. Meng M, Wang J, Huang H, et al. 3D printing metal implants in orthopedic surgery: Methods, applications and future prospects. *Journal of Orthopaedic Translation* 2023; 42: 94-112. https://doi.org/10.1016/j.jot.2023.08.004.

13. Li J, Cui X, Hooper GJ, et al. Rational design, bio-functionalization and biological performance of hybrid additive manufactured titanium implants for orthopaedic applications: A review. *Journal of the Mechanical Behavior of Biomedical Materials* 2020; 105: 103671. https://doi.org/10.1016/j.jmbbm.2020.103671.

14. Chen Z, Chen Y, Ding J, et al. Blending strategy to modify PEEK-based orthopedic implants. *Composites Part B: Engineering* 2023; 250: 110427. https://doi.org/10.1016/j.compositesb.2022.110427.

15. Ma H, Suonan A, Zhou J, et al. PEEK (Polyether-ether-ketone) and its composite materials in orthopedic implantation. *Arabian Journal of Chemistry* 2021; 14: 102977. https://doi.org/10.1016/j.arabjc.2020.102977.

16. Saini A, Elhattab K, Gummadi SK, et al. Fused filament fabrication-3D printing of poly-ether-ether-ketone (PEEK) spinal fusion cages. *Materials Letters* 2022; 328: 133206. https://doi.org/10.1016/j.matlet.2022.133206.

17. Canseco JA, Karamian BA, DiMaria SL, et al. Static Versus Expandable Polyether Ether Ketone (PEEK) Interbody Cages: A Comparison of One-Year Clinical and Radiographic Outcomes for One-Level Transforaminal Lumbar Interbody Fusion. *World Neurosurgery* 2021; 152: e492-e501. https://doi.org/10.1016/j.wneu.2021.05.128.

18. Sahoo PK. Polyetheretherketone (PEEK) cages for cervical interbody replacement. *Apollo Medicine* 2013; 10: 233-236. https://doi.org/10.1016/j.apme.2013.08.009.

19. Zhang Q, Sun C, Zheng J, et al. Mechanical behaviour of additive manufactured PEEK/HA porous structure for orthopaedic implants: Materials, structures and manufacturing processes. *Journal of the Mechanical Behavior of Biomedical Materials* 2025; 163: 106848. https://doi.org/10.1016/j.jmbbm.2024.106848.

20. Li Q, Hu B, Wang L, et al. Biomineralized PEEK cages containing osteoinductive CaP bioceramics promote spinal fusion in goats. *Bioactive Materials* 2025; 45: 128-147. https://doi.org/10.1016/j.bioactmat.2024.11.014.

21. Zhang H, Guo Z, Zhang Z, et al. Biomimetic design and fabrication of PEEK and PEEK/CF cage with minimal surface structures by fused filament fabrication. *Journal of Materials Research and Technology* 2023; 26: 5001-5015.

https://doi.org/10.1016/j.jmrt.2023.08.236.

22. Bencharit S, Byrd WC, Altarawneh S, et al. Development and Applications of Porous Tantalum Trabecular Metal-Enhanced Titanium Dental Implants. *Clinical Implant Dentistry and Related Research* 2014; 16: 817-826. https://doi.org/10.1111/cid.12059.

23. Piglionico S, Bousquet J, Fatima N, et al. Porous Tantalum vs. Titanium Implants: Enhanced Mineralized Matrix Formation after Stem Cells Proliferation and Differentiation. *Journal of Clinical Medicine* 2020; 9. https://doi.org/10.3390/jcm9113657.

24. Li X, Wang L, Yu XM, et al. Tantalum coating on porous Ti6Al4V scaffold using chemical vapor deposition and preliminary biological evaluation. *Materials Science & Engineering C-Materials for Biological Applications* 2013; 33: 2987-2994. https://doi.org/10.1016/j.msec.2013.03.027.

25. Wang X, Ning B and Pei X. Tantalum and its derivatives in orthopedic and dental implants: Osteogenesis and antibacterial properties. *Colloids and Surfaces B: Biointerfaces* 2021; 208: 112055. https://doi.org/10.1016/j.colsurfb.2021.112055.

26. Ataee A, Li Y, Brandt M, et al. Ultrahigh-strength titanium gyroid scaffolds manufactured by selective laser melting (SLM) for bone implant applications. *Acta Materialia* 2018; 158: 354-368. https://doi.org/10.1016/j.actamat.2018.08.005.

27. Zhang Y, Yang J, Wan W, et al. Evaluation of biological performance of 3D printed trabecular porous tantalum spine fusion cage in large animal models. *Journal of Orthopaedic Translation* 2025; 50: 185-195. https://doi.org/10.1016/j.jot.2024.10.010.

28. Chen J, Song C, Deng Z, et al. Functional gradient design of additive manufactured gyroid tantalum porous structures: Manufacturing, mechanical behaviors and permeability. *Journal of Manufacturing Processes* 2024; 125: 202-216. https://doi.org/10.1016/j.jmapro.2024.07.054.

29. Gao HR, Yang JZ, Jin X, et al. Porous tantalum scaffolds: Fabrication, structure, properties, and orthopedic applications. *Materials & Design* 2021; 210. https://doi.org/10.1016/j.matdes.2021.110095.

30. Chen LY, Liang SX, Liu YJ, et al. Additive manufacturing of metallic lattice

structures: Unconstrained design, accurate fabrication, fascinated performances, and challenges. *Materials Science & Engineering R-Reports* 2021; 146. https://doi.org/10.1016/j.mser.2021.100648.

31. Benedetti M, du Plessis A, Ritchie RO, et al. Architected cellular materials: A review on their mechanical properties towards fatigue-tolerant design and fabrication. *Materials Science & Engineering R-Reports* 2021; 144. https://doi.org/10.1016/j.mser.2021.100606.

32. G G, Reddy NDD, Penumakala PK, et al. Compressive response of additively manufactured Ti–6Al–4V Triply Periodic Minimal Surface structures with different unit cell designs for biomedical implant applications. *Materials Today Communications* 2025; 44: 112013. https://doi.org/10.1016/j.mtcomm.2025.112013.

33. Araya M, Jaskari M, Rautio T, et al. Assessing the compressive and tensile properties of TPMS-Gyroid and stochastic Ti64 lattice structures: A study on laser powder bed fusion manufacturing for biomedical implants. *Journal of Science: Advanced Materials and Devices* 2024; 9: 100663. https://doi.org/10.1016/j.jsamd.2023.100663.

34. Zhang J, Shen Y, Sun Y, et al. Design and mechanical testing of porous lattice structure with independent adjustment of pore size and porosity for bone implant. *Journal of Materials Research and Technology* 2022; 18: 3240-3255. https://doi.org/10.1016/j.jmrt.2022.04.002.

35. Perets T, Ben Ghedalia-Peled N, Vago R, et al. In vitro behavior of bioactive hybrid implant composed of additively manufactured titanium alloy lattice infiltrated with Mg-based alloy. *Materials Science and Engineering C-Materials for Biological Applications* 2021; 129. https://doi.org/10.1016/j.msec.2021.112418.

36. Lei PF, Qian H, Zhang TM, et al. Porous tantalum structure integrated on Ti6Al4V base by Laser Powder Bed Fusion for enhanced bony-ingrowth implants: In vitro and in vivo validation. *Bioactive Materials* 2022; 7: 3-13. https://doi.org/10.1016/j.bioactmat.2021.05.025.

37. Wang Y-T and Hsu C-K. Novel parameter optimization lattice design for improving osseointegration in hypo-loading regions – A case study of maxillary tumor

reconstruction implant. *Materials & Design* 2023; 233: 112274. https://doi.org/10.1016/j.matdes.2023.112274.

38. Fengbin Y, Jinhao M, Xinyuan L, et al. Evaluation of a new type of titanium mesh cage versus the traditional titanium mesh cage for single-level, anterior cervical corpectomy and fusion. *European Spine Journal* 2013; 22: 2891-2896. https://doi.org/10.1007/s00586-013-2976-1.

39. Buttermann GR, Freeman AL and Beaubien BP. In vitro biomechanics of an expandable vertebral body replacement with self-adjusting end plates. *The Spine Journal* 2010; 10: 1024-1031. https://doi.org/10.1016/j.spinee.2010.08.017.

40. Chen G, Yin M, Liu W, et al. A Novel Height-Adjustable Nano-Hydroxyapatite/Polyamide-66 Vertebral Body for Reconstruction of Thoracolumbar Structural Stability After Spinal Tumor Resection. *World Neurosurgery* 2019; 122: e206-e214. https://doi.org/10.1016/j.wneu.2018.09.213.

41. du Plessis A, Razavi SMJ, Benedetti M, et al. Properties and applications of additively manufactured metallic cellular materials: A review. *Progress in Materials Science* 2022; 125. https://doi.org/10.1016/j.pmatsci.2021.100918.

42. Zhang YT, Aiyiti W, Du S, et al. Design and mechanical behaviours of a novel tantalum lattice structure fabricated by SLM. *Virtual and Physical Prototyping* 2023; 18: e2192702. https://doi.org/10.1080/17452759.2023.2192702.

43. Zhang Y, Aiyiti W, Li J, et al. Innovative design and compression performance of selective laser melting-printed tantalum artificial vertebral bodies. *IJB* 2025. https://doi.org/10.36922/ijb025150133.

44. Zhou E, Huang H, Zhao Y, et al. The effects of titanium mesh cage size on the biomechanical responses of cervical spine after anterior cervical corpectomy and fusion: A finite element study. *Clinical Biomechanics* 2022; 91: 105547. https://doi.org/10.1016/j.clinbiomech.2021.105547.

45. Hua W, Zhi J, Wang B, et al. Biomechanical evaluation of adjacent segment degeneration after one- or two-level anterior cervical discectomy and fusion versus cervical disc arthroplasty: A finite element analysis. *Computer Methods and Programs in Biomedicine* 2020; 189: 105352. https://doi.org/10.1016/j.cmpb.2020.105352.

46. Yuan W, Zhang H, Zhou X, et al. The Influence of Artificial Cervical Disc Prosthesis Height on the Cervical Biomechanics: A Finite Element Study. *World Neurosurgery* 2018; 113: e490-e498. https://doi.org/10.1016/j.wneu.2018.02.062.

47. Zhao L, Chen J, Liu J, et al. Biomechanical analysis on of anterior transpedicular screw-fixation after two-level cervical corpectomy using finite element method. *Clinical Biomechanics* 2018; 60: 76-82. https://doi.org/10.1016/j.clinbiomech.2018.09.008.

48. Wu T-k, Meng Y, Liu H, et al. Biomechanical effects on the intermediate segment of noncontiguous hybrid surgery with cervical disc arthroplasty and anterior cervical discectomy and fusion: a finite element analysis. *The Spine Journal* 2019; 19: 1254-1263. https://doi.org/10.1016/j.spinee.2019.02.004.

49. Sun B, Han Q, Sui F, et al. Biomechanical analysis of customized cage conforming to the endplate morphology in anterior cervical discectomy fusion: A finite element analysis. *Heliyon* 2023; 9: e12923. https://doi.org/10.1016/j.heliyon.2023.e12923.

50. Clausen JD, Goel VK, Traynelis VC, et al. Uncinate processes and Luschka joints influence the biomechanics of the cervical spine: Quantification using a finite element model of the C5-C6 segment. *Journal of Orthopaedic Research* 1997; 15: 342-347. https://doi.org/10.1002/jor.1100150305.

51. Jonas R, Demmelmaier R and Wilke H-J. Influences of functional structures on the kinematic behavior of the cervical spine. *The Spine Journal* 2020; 20: 2014-2024. https://doi.org/10.1016/j.spinee.2020.07.017.

52. Li Z, Liu H, Yang M, et al. A biomechanical analysis of four anterior cervical techniques to treating multilevel cervical spondylotic myelopathy: a finite element study. *BMC Musculoskeletal Disorders* 2021; 22: 278. https://doi.org/10.1186/s12891-021-04150-7.

53. Lin M, Shapiro SZ, Doulgeris J, et al. Cage-screw and anterior plating combination reduces the risk of micromotion and subsidence in multilevel anterior cervical discectomy and fusion—a finite element study. *The Spine Journal* 2021; 21: 874-882. https://doi.org/10.1016/j.spinee.2021.01.015.

54. Panjabi MM, Crisco JJ, Vasavada A, et al. Mechanical Properties of the Human

Cervical Spine as Shown by Three-Dimensional Load–Displacement Curves. *Spine* 2001; 26: 2692-2700.

55. Lee S-H, Im Y-J, Kim K-T, et al. Comparison of Cervical Spine Biomechanics After Fixed- and Mobile-Core Artificial Disc Replacement: A Finite Element Analysis. *Spine* 2011; 36: 700-708. https://doi.org/10.1097/BRS.0b013e3181f5cb87.

56. Lee JH, Park WM, Kim YH, et al. A Biomechanical Analysis of an Artificial Disc With a Shock-absorbing Core Property by Using Whole-cervical Spine Finite Element Analysis. *Spine* 2016; 41: E893-E901. https://doi.org/10.1097/brs.0000000000001468.

57. Yu C-C, Liu P, Huang D-G, et al. A new cervical artificial disc prosthesis based on physiological curvature of end plate: a finite element analysis. *The Spine Journal* 2016; 16: 1384-1391. https://doi.org/10.1016/j.spinee.2016.06.019.

58. Liu N, Lu T, Wang Y, et al. Effects of New Cage Profiles on the Improvement in Biomechanical Performance of Multilevel Anterior Cervical Corpectomy and Fusion: A Finite Element Analysis. *World Neurosurgery* 2019; 129: e87-e96. https://doi.org/10.1016/j.wneu.2019.05.037.

59. Kallemeyn N, Gandhi A, Kode S, et al. Validation of a C2–C7 cervical spine finite element model using specimen-specific flexibility data. Medical Engineering & Physics 2010; 32: 482-489. https://doi.org/10.1016/j.medengphy.2010.03.001.